Construction and Building Materials 541 (2026) 147691

Contents lists available at ScienceDirect

Construction and Building Materials

journal homepage: www.elsevier.com/locate/conbuildmat

Rheology and CFD-based spreading of cementitious mortars with ornamental rock processing fines: Effective Herschel–Bulkley parameterization and calibrated free-spreading benchmark

M.T. Gabriel [a,*], A.V. Bahiense [b], G.C. Xavier [c], L.M. Fernandes [b], V.P. Della Sagrillo [a], M.A. Rabbi [d]

[a] PROPEMM, Instituto Federal do Espírito Santo (IFES), Vitória, ES, Brazil
[b] Instituto Federal do Espírito Santo (IFES), Cachoeiro de Itapemirim, ES, Brazil
[c] Centro de Ciência e Tecnologia, Universidade Estadual Norte Fluminense Darcy Ribeiro (UENF), Campos dos Goytacazes, RJ, Brazil
[d] Instituto Capixaba de Gestão, Cachoeiro de Itapemirim, ES, Brazil

ARTICLE INFO

Dataset link: https://doi.org/10.17632/vfxk7tfzxg.1

Keywords:
Cement mortar
Ornamental rock fines
Effective rheological parameters
Squeeze-flow
CFD
OpenFOAM
Herschel–Bulkley

ABSTRACT

This study investigates the influence of ornamental rock processing fines (FIBRO) on the fresh-state behavior of cementitious mortars by combining fresh-state testing, squeeze-flow-based rheological parameterization, and OpenFOAM simulations of gravity-driven free spreading. Reference and FIBRO-containing mortars were prepared at five water-to-cement ratios and evaluated by fresh density, flow-table consistency, and instrumented squeeze-flow tests. Force–displacement curves were interpreted using a Roussel–Muravleva-based approach to obtain effective Herschel–Bulkley parameters (τ_0, K, and n) for CFD input. The FIBRO series showed a higher descriptive mean fresh density (2327 kg m^{-3}) than the reference series (1982 kg m^{-3}) and reached the target terminal spread of 260 mm with an approximately 4.2% lower w/c ratio. All mixtures showed strongly shear-thinning behavior, with flow-index values close to 0.5. After calibration at t = 15 s, the simulations reproduced the early free-spreading stage but progressively overestimated radius and underestimated height between 30 and 60 s. Because the model does not include flow-table impacts, the comparison is interpreted as a calibrated free-spreading benchmark rather than a full time-resolved validation of the standardized consistency test. Late-stage deviations may reflect constitutive simplification, numerical regularization, experimental–numerical non-equivalence, and possible time-dependent structural evolution. The results support FIBRO as a promising waste-valorization route for fresh mortars while defining the limits of stationary Herschel–Bulkley CFD extrapolation.

1. Introduction

The construction industry consumes large volumes of natural resources, particularly fine aggregates and mineral binders, a practice that generates substantial environmental impacts and increases pressure on natural deposits. The extraction of sand and crushed stone has been subject to regulatory and socio-environmental constraints, increasing costs and encouraging the search for alternative raw materials with a lower environmental burden. In parallel, ornamental rock processing generates large amounts of fines, here referred to as FIBRO (ornamental rock processing fines), a residue with environmental pollution potential and high disposal costs [1]. The incorporation of FIBRO into cementitious composites therefore emerges as a promising strategy to reduce the demand for natural raw materials and redirect an abundant waste stream toward higher value-added applications, provided that adequate fresh-state performance can be ensured.

According to NBR 15012 (2013) [2], ornamental rock comprises natural stone materials used for cladding and architectural elements, including both carbonate and siliceous rocks. FIBRO corresponds to the fines generated during the cutting, grinding, and polishing of these materials and is typically composed of rock powder and small fractions of processing inputs [1,3]. Previous characterization studies have reported compositions that vary with the processed rock types: quartz- and dolomite-rich fines have been reported [4], whereas fines derived from granite/gneiss processing show silicate assemblages dominated by quartz, feldspars, and micas [5,6]. Ornamental rock waste is commonly used as a mineral filler in cementitious materials because

* Corresponding author.
E-mail address: marcostgabriel@yahoo.com.br (M.T. Gabriel).

https://doi.org/10.1016/j.conbuildmat.2026.147691
Received 13 May 2026; Received in revised form 8 July 2026; Accepted 2 August 2026
Available online 19 August 2026
0950-0618/© 2026 Published by Elsevier Ltd.

of its fine particle-size distribution; Bahiense et al. [7] reported waste fines with D_{50} = 10.7 μm and a fineness modulus of 0.30, while Amaral et al. [8] reported more than 90% of particles below 0.075 mm. This fine particle-size distribution supports the use of ornamental rock waste as a filler, potentially favoring void filling and a denser granular arrangement when the water content is properly adjusted. Such changes in the granular skeleton are expected to affect water demand and fresh-state behavior, including workability and rheological response [9].

In rendering mortars, fresh-state behavior is governed by the interaction among fine aggregate, binder, water content, and mineral additions. When fine mineral residues are incorporated, particle-size distribution and surface characteristics become particularly relevant, since they affect particle packing, available water, and interparticle lubrication. These effects can modify both workability and the rheological response of the mixture, especially when the water content is adjusted to achieve a target consistency [7,9].

In practical mix design, however, there is still no universally established rational procedure for mortars. For this reason, many studies and technical practices rely on experimental iteration, initially selecting a water-to-cement ratio (w/c) and then adjusting the relative proportions of binders and aggregates until the desired workability is obtained [7, 10]. Workability, defined in standards and recent studies as the ability of mortar to be mixed, placed, and spread without segregation [9,11], is still often assessed on site by empirical judgment based on the worker's handling of the material. Empirical mix-design procedures may obscure the relationship between water content, particle-size distribution, fresh density, and fresh-state performance, especially when mineral fines are incorporated into cementitious materials. Rational mix-design approaches should therefore consider particle-size distribution, fresh density, and water-to-cement ratio [7]. Reviews and experimental studies indicate that workability should instead be interpreted through measurable rheological parameters, especially yield stress and plastic viscosity, obtained from tests such as flow-table, cone, vane, and rheometer tests [12]. For rendering and laying mortars, NBR 15839 (2010) [13] recommends a combination of low plastic viscosity, to reduce spreading effort, and sufficiently high yield stress, to prevent sagging.

Within the sustainability context, the literature on ornamental rock residues in cementitious composites has mainly reported effects on mechanical performance and environmental indicators. Studies on ornamental stone waste, marble powder, and granite powder have shown that partial replacement of cement or fine aggregate can preserve or improve fresh-state and mechanical performance, depending on residue characteristics and replacement level, while also contributing to lower environmental impacts [14–18]. In cementitious systems containing ornamental rock waste, previous studies have shown that its effect depends strongly on the replacement level and application route. Low cement-replacement levels may preserve fresh-state performance and mechanical strength, whereas higher cement-replacement levels tend to impair workability and strength [14,19]. For sand replacement in mortars, contents around 30 wt% have shown favorable mechanical and environmental performance, although the response depends on cement type, curing age, and residue characteristics [18]. For cement replacement, ornamental stone waste contents close to 10 wt% have been reported to provide fresh and hardened properties comparable to plain Portland cement pastes, whereas higher replacement levels tend to reduce compressive strength [14,19].

In parallel, computational simulation and advanced rheological approaches are increasingly used to describe the flow of pastes, concretes, and mortars through Bingham- and Herschel–Bulkley-type models regularized for computational fluid dynamics (CFD) [20–22]. Recent studies using OpenFOAM and ANSYS Fluent have reproduced slump-flow and mini-slump tests with small errors in spreading radius, discussed the role of mold lifting velocity, and compared different regularization schemes [23–26]. The practical consequences of rheological-model selection and of the shear-rate window used for parameter fitting have also been quantified in other yield-stress spreading problems, such as cement grout propagation in rock fractures, where they modify predicted propagation lengths and filling ratios by tens of percent [27,28]. Nevertheless, despite the progress achieved in numerical simulation and in the experimental study of fresh cementitious materials, the integration of ornamental rock residues, rheological characterization, and CFD-based prediction of gravity-driven spreading remains limited.

Despite recent advances in the incorporation of mineral residues into cementitious materials, significant gaps remain in understanding fresh-state rheological behavior when experimental workability tests are combined with numerical simulation. Most studies on ornamental stone waste, marble powder, and granite powder have focused on cement or aggregate replacement, mechanical performance, durability, or environmental indicators. Comparatively less attention has been given to the combined use of fresh-state measurements, squeeze-flow-based effective rheological fitting, and CFD-based analysis of mortar spreading. This gap is particularly relevant for rendering mortars, in which workability is not governed by spread diameter alone, but by the coupled effects of water demand, fresh density, yield stress, viscosity, cohesion, and application performance.

In this context, this study investigates the influence of ornamental rock processing fines (FIBRO) on the fresh-state behavior of cementitious mortars through an integrated experimental and numerical approach. In the formulation adopted here, FIBRO replaces hydrated lime rather than cement or sand; therefore, the results must be interpreted within this specific mix-design route, in which changes in water retention, cohesion, and plasticity may accompany the filler effect commonly associated with fine mineral residues. The specific objectives are: (i) to quantify the water demand required to achieve a target terminal spread in reference and FIBRO-containing mortars; (ii) to evaluate the fresh density and consistency response of the two series as composition-specific trends; (iii) to derive effective Herschel–Bulkley parameters from squeeze-flow tests, recognizing that these parameters are not intrinsic material constants; and (iv) to assess the ability and limitations of OpenFOAM simulations to reproduce gravity-driven free spreading after calibration.

The working assumptions examined in this study are: (i) the fine particle-size distribution of FIBRO, together with the measured fresh-density response, is consistent with a denser granular arrangement and reduced water demand, although direct particle-shape and microstructural characterization is still required to confirm the underlying mechanisms; (ii) replacing hydrated lime with FIBRO modifies the effective rheological response while still allowing the target workability to be reached; and (iii) a stationary Herschel–Bulkley model can provide a useful calibrated benchmark for early-stage gravity-driven spreading, but late-stage extrapolation must be interpreted cautiously because it may be affected by numerical regularization, the absence of flow-table impacts in the CFD model, and possible time-dependent structural evolution of the mortar.

2. Materials and methods

2.1. Rheological model, regularization, and effective parameter estimation

The Herschel–Bulkley (HB) model was adopted because it has been widely used to represent yield-stress, shear-thinning cementitious materials and has been reported to be suitable for simulating mortar flow behavior [29]. In the present work, however, the HB parameters are treated as effective parameters derived from squeeze-flow tests rather than as intrinsic material constants. This distinction is important because squeeze-flow imposes a heterogeneous deformation field, combining extensional and shear components, and does not replace full rotational rheometry. The objective of the parameterization is therefore

to provide a reproducible set of inputs for the CFD simulations, not to establish universal constitutive constants for the mortars.

For yielded material, the scalar form of the model is given by Eq. (1):

$$\tau = \tau_0 + K\,|\dot{\gamma}|^n \tag{1}$$

where τ is the shear stress [Pa], τ_0 is the effective yield-stress parameter [Pa], K is the effective consistency index [Pa s^n], n is the flow index [-], and $\dot{\gamma}$ is the shear rate [s^{-1}].

To avoid numerical divergence at very low shear rates ($|\dot{\gamma}| \to 0$), a viscosity plateau μ_0 was imposed [21], as shown in Eq. (2). This approach is a practical bi-viscosity regularization of the HB law and differs from Papanastasiou-type exponential regularization [30,31].

$$\mu_{\text{eff}}(|\dot{\gamma}|) = \min\left\{\mu_0,\ \frac{\tau_0}{|\dot{\gamma}|} + K\,|\dot{\gamma}|^{n-1}\right\} \tag{2}$$

The plateau viscosity μ_0 is not interpreted here as an independently measured material property. It is a numerical regularization parameter introduced to limit the apparent viscosity when the shear rate approaches zero. Therefore, low-shear regions may continue to deform slowly under the imposed viscosity cap, and late-stage spreading can be affected by residual numerical creep. Since no independent sensitivity analysis of μ_0 was performed in the present study, deviations observed at longer simulation times are not attributed exclusively to mortar thixotropy or structural build-up; instead, they are interpreted as the combined outcome of constitutive simplification, numerical regularization, and experimental–numerical non-equivalence.

In OpenFOAM, the `HerschelBulkley` model implements viscosity in kinematic form by dividing the dynamic viscosity by the density ρ, as expressed in Eq. (3):

$$\nu(|\dot{\gamma}|) = \min\left(\nu_0,\ \frac{\tau_0}{\rho\,|\dot{\gamma}|} + \frac{K}{\rho}\,|\dot{\gamma}|^{n-1}\right), \tag{3}$$

where ρ is the fresh density [kg m^{-3}] and $\nu_0 = \mu_0/\rho$ is the low-shear-rate kinematic viscosity [m^2 s^{-1}]. To define the model in the `momentumTransport` dictionary, the quantities `tau0` $= \tau_0/\rho$, `k` $= K/\rho$, and `n` $= n$ are specified directly, as recommended in the OpenFOAM user guide [32]. The origin of the parameters used in the CFD simulations is described in Sections 2.2 and 2.3, and the numerical setup is detailed in Section 2.6.

2.2. Roussel-based estimate of the effective yield-stress parameter

For yield-stress materials, Roussel et al. [33] proposed a relationship between the yield stress and the spread radius measured in slump-type tests. In the form employed by Thiedeitz et al. [21], based on Roussel's formulation, the analytical estimate is given by Eq. (4):

$$\tau_{0,\text{A,R}} \approx \frac{225\,\rho\,g\,V^2}{128\,\pi^2\,R^5}, \tag{4}$$

where ρ is the fresh density [kg m^{-3}], g is the gravitational acceleration [m s^{-2}], V is the initial volume [m^3], and R is the reference spread radius [m].

In the present work, Eq. (4) was used to obtain a Roussel-based estimate of the effective yield-stress parameter, not a direct independent measurement of the intrinsic yield stress. This distinction is important because the Roussel relationship is based on gravity-driven slump-type spreading, whereas the NBR 13276 flow-table test [34] provides a final dynamic workability index obtained after mold removal and prescribed table jolting. Therefore, the final post-jolting consistency diameter was not used to calculate $\tau_{0,\text{A,R}}$.

Instead, the radius R used in Eq. (4) was taken from the post-mold geometric reference extracted from the first video frame immediately after vertical mold removal and before the application of the 30 table drops. This choice was adopted because the post-mold state is the closest experimental reference available to the gravity-driven free-spreading condition represented in the CFD simulations. Consequently, the resulting $\tau_{0,\text{A,R}}$ values are interpreted as effective estimates used to anchor the squeeze-flow parameterization and the CFD input set. They should not be interpreted as direct rheometric measurements or as yield-stress values inferred from the final post-jolting consistency diameter.

Table 1
Geometry check for the Roussel-based estimate using the post-mold reference radius.

Mix	R_{pm} (mm)	h_{eq} (mm)	$h_{\text{eq}}/R_{\text{pm}}$
R30	62.5	44.4	0.711
R40	62.5	44.4	0.711
R50	67.0	38.6	0.577
R60	72.0	33.5	0.465
R70	73.5	32.1	0.437
F30	62.5	44.4	0.711
F40	64.5	41.7	0.646
F50	68.0	37.5	0.552
F60	75.5	30.4	0.403
F70	63.5	43.0	0.677

R_{pm} is the post-mold reference radius measured from the first video frame immediately after vertical mold removal and before table jolting. The equivalent thickness h_{eq} was estimated from volume conservation using the NBR 13276 truncated-cone volume, $V = 5.44968 \times 10^{-4}$ m^3.

The cone specified in NBR 13276 (2016) [34] was represented by a truncated cone with bottom diameter $D_b = 125$ mm, top diameter $D_t = 80$ mm, and height $h = 65$ mm. The volume of the truncated cone is calculated by Eq. (5):

$$V = \frac{\pi h}{12}\left(D_b^2 + D_b D_t + D_t^2\right), \tag{5}$$

which, for these values, gives $V = 5.44968 \times 10^{-4}$ m^3. This value was used in Eq. (4) for all mixtures.

Because the Roussel relationship is derived under simplified spreading assumptions, its applicability depends on the geometry used in the estimate. To make this limitation explicit, an equivalent thickness-to-radius ratio was estimated from volume conservation as:

$$\frac{h_{\text{eq}}}{R_{\text{pm}}} = \frac{V}{\pi R_{\text{pm}}^3}, \tag{6}$$

where R_{pm} is the post-mold reference radius and h_{eq} is the equivalent thickness obtained by distributing the truncated-cone volume over a circular area of radius R_{pm}.

The resulting $h_{\text{eq}}/R_{\text{pm}}$ values (Table 1) range from 0.403 to 0.711. These values indicate that the post-mold geometries do not fully satisfy a very thin-layer asymptotic regime. Therefore, the Roussel-based values are used here only as effective estimates for parameter initialization and CFD input consistency, not as direct rheometric measurements. This limitation reinforces the need to interpret $\tau_{0,\text{A,R}}$ as an effective parameter tied to the adopted experimental–numerical workflow rather than as an intrinsic material constant.

2.3. Squeeze-flow force model and extraction of effective Herschel–Bulkley parameters

Instrumented squeeze-flow tests were used to obtain an effective rheological parameterization compatible with the force–displacement response of each mortar. The procedure follows the lubrication-based interpretation of squeeze flow for yield-stress fluids [20,35,36], while recognizing that the test imposes a non-uniform deformation field, with combined extensional and shear components. Therefore, the parameters extracted from this procedure are treated as effective Herschel–Bulkley parameters for CFD input, not as intrinsic material constants.

We consider axisymmetric compression between parallel plates with one plate moving at constant velocity v (kinematics $2U = v$). Let

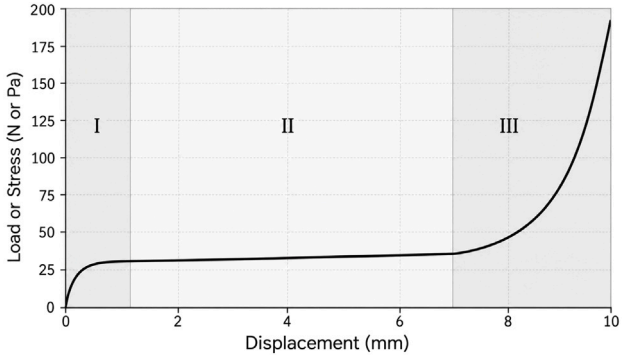


Fig. 1. Idealized squeeze-flow force–displacement curve showing the three deformation regimes used to define the fitting interval. Phase I corresponds to the initial contact/transient stage, Phase II to the lubrication-dominated regime, and Phase III to the final force rise as the gap decreases. Only Phases II–III were used for effective Herschel–Bulkley parameter fitting.

$R(t)$ be the instantaneous radius, $A(t)$ the instantaneous area, $h(t)$ the instantaneous gap, V_s the specimen volume, $\Delta(t)$ the measured axial displacement, and h_0 the initial plate spacing. By conservation of volume, the relations in Eq. (7) hold:

$$R(t) = \sqrt{\frac{V_s}{\pi h(t)}}, \qquad A(t) = \pi R(t)^2 = \frac{V_s}{h(t)}, \qquad h(t) = h_0 - \Delta(t). \tag{7}$$

In the thin-film regime with full adhesion at the plates (no-slip condition), the asymptotic solution of Muravleva [35] for the force of a Herschel–Bulkley fluid can be written, over a wide range of effective Bingham numbers, as the sum of a yield contribution and a viscous contribution:

$$F(h; v, \tau_0, K, n) = \left(\frac{V_s}{\pi}\right)^{3/2} \left[C_y(n)\,\tau_0\,h^{-5/2} + C_v(n)\,K\,v^n\,h^{-(n+5/2)}\right], \tag{8}$$

where F is the axial force, τ_0 is the effective yield-stress parameter, K is the effective consistency index, n is the flow index, and $C_y(n)$ and $C_v(n)$ are asymptotic coefficients of order $\mathcal{O}(1)$ in the formulation of Muravleva [35]. In practice, the theoretical values of C_y and C_v may be used directly, or they may be absorbed into effective parameters $\tau_0^* = C_y(n)\tau_0$ and $K^* = C_v(n)K$ without changing the curve shape or the coefficient of determination. For this reason, the fitted values reported in this work should be interpreted as test-dependent effective parameters suitable for numerical parameterization.

The experimental $F(\Delta)$ curve typically exhibits three regimes: (I) an initial transient/contact-adjustment stage, (II) a quasi-steady lubrication-dominated range, and (III) a sharp force increase as the gap decreases (Fig. 1). Because Eq. (8) is based on the thin-film lubrication regime, the fitting procedure was restricted to Phases II–III. The boundaries between the three regimes were identified from the derivative of the smoothed force–displacement curve using a Savitzky–Golay filter. Fig. 1 is an idealized schematic representation of the fitting logic adopted in this work, rather than a direct experimental curve for a specific mixture.

Small gap and compliance effects were represented by a velocity-dependent displacement offset $d_{0,j}$, where j denotes the imposed velocity. The corrected gap used internally in the model calculation was:

$$h = h_0 - \left(\Delta - d_{0,j}\right). \tag{9}$$

The zero offset was estimated during the initial stage of the fit and applied only to the model calculations. The plots in this paper always display the raw displacement axis Δ, without translation, to preserve the displacement actually measured by the actuator.

The standard velocities $v \in \{0.1, 3.0\}$ mm s^{-1} were used, following NBR 15839 [13]. For each mixture, the Roussel-based value $\tau_{0,A,R}$ obtained from Eq. (4) was used as the initial estimate and reference value for the effective yield-stress parameter. The squeeze-flow fitting was then used to obtain a consistent set of effective parameters compatible with the curves measured at both velocities. This procedure makes explicit the connection between the post-mold geometric reference, the Roussel-based yield-stress estimate, the squeeze-flow response, and the CFD input parameters.

The fitting workflow was as follows:

1. **Roussel-based yield-stress estimate:** the post-mold reference radius and fresh density were used to calculate $\tau_{0,A,R}$ according to Eq. (4). This value was treated as an effective estimate and reference for the yield contribution in Eq. (8).
2. **Selection of the usable squeeze-flow interval:** the initial contact/transient stage was excluded, and the fitting interval was restricted to Phases II–III, identified from the derivative of the smoothed force–displacement curve.
3. **Offset correction:** velocity-dependent offsets $d_{0,j}$ were estimated to account for small gap and compliance effects, using Eq. (9). These offsets were applied only within the model calculation.
4. **Flow-index profiling and consistency fitting:** the flow index n was swept within a physically plausible shear-thinning range. For each candidate value of n, the effective consistency index K was fitted by least squares using the curves obtained at 0.1 and 3.0 mm s^{-1}, while maintaining consistency with the Roussel-based yield-stress estimate.
5. **Final parameter selection:** the final value of n was selected from the best global fit considering both velocities simultaneously. The final set of τ_0, K, and n was then used as the effective Herschel–Bulkley parameterization for the CFD simulations.

The coefficient of determination R^2 is reported for each velocity and for the global fit as a descriptive indicator of fitting quality. It should not be interpreted as inferential statistical validation of a universal constitutive model, because independent replicate batches were not available for all responses and because squeeze-flow does not impose a homogeneous shear field. The final parameter set is therefore a practical effective parameterization linking the measured fresh-state response, the squeeze-flow curves, and the CFD simulations. The provenance of the final parameters used in OpenFOAM is summarized together with the numerical inputs in Table 2.

2.4. Mortars and mix proportions

Two mortar series were produced: a reference series (R) and a FIBRO-containing series (F). The dry mass proportion adopted for the reference mortar was 1:1:6, corresponding to hydrated lime, Portland cement, and sand, respectively. This proportion is commonly used as a practical reference for rendering mortars and provides a suitable basis for comparing the effect of replacing the lime fraction in the fresh-state response.

In the FIBRO-containing series, the hydrated lime fraction was fully replaced by ornamental rock processing fines, while the cement and sand contents were kept unchanged. Therefore, FIBRO was not used as a cement replacement or as a sand replacement in this study. This methodological choice is important because hydrated lime contributes to plasticity, cohesion, water retention, and application performance in rendering mortars. Consequently, the comparison between the R and F series should be interpreted within this specific mix-design route, in which the replacement of lime by a fine mineral residue may simultaneously alter particle packing, available water, cohesion, and the effective rheological response.

The constituent materials were selected according to the relevant Brazilian standards, as summarized in Table 3. Since no specific Brazilian standard applies to FIBRO as a mortar constituent, the material was identified as an ornamental rock processing fine and characterized

Table 2
Effective rheological parameters and OpenFOAM input values used for each mortar mixture.

Mix	ρ	$\tau_{0,A,R}$	$\tau_{0,CFD}$	K	n	ν_0	τ_0/ρ	$k = K/\rho$	$R^2_{0.1}$	$R^2_{3.0}$	R^2_{glob}
	kg m^{-3}	Pa	Pa	Pa s^n	–	m^2 s^{-1}	m^2 s^{-2}	m^2 s^{n-2}	–	–	–
R30	1891	1029	1029	104.17	0.570	15.9199	0.543014	0.055070	0.9898	0.9828	0.9862
R40	1923	1046	1046	122.36	0.578	87.5559	0.543417	0.063636	0.9800	0.9652	0.9741
R50	1982	762	762	171.62	0.541	2.23267	0.384471	0.086568	0.9906	0.9804	0.9862
R60	2036	546	546	211.55	0.517	1.06119	0.268260	0.103901	0.9954	0.9876	0.9926
R70	2050	496	496	203.52	0.541	1.00722	0.241463	0.099771	0.9987	0.9953	0.9972
F30	2356	1282	1282	164.53	0.510	38.9466	0.544216	0.069850	0.9977	0.9919	0.9912
F40	2330	1083	1083	295.61	0.538	4.45793	0.464378	0.126809	0.9475	0.8767	0.9457
F50	2327	830	830	315.54	0.515	2.03876	0.356872	0.135641	0.9772	0.8773	0.9550
F60	2322	491	491	379.28	0.542	0.86545	0.211400	0.163436	0.9773	0.9567	0.9706
F70	2281	1146	1146	179.11	0.537	6.46802	0.502411	0.078522	0.9902	0.9860	0.9900

$\tau_{0,A,R}$ denotes the Roussel-based effective yield-stress estimate obtained from the post-mold reference radius measured immediately after mold removal and before table jolting. This radius was adopted because the Roussel relationship is based on gravity-driven slump-type spreading and is not directly equivalent to the dynamically excited final spread of the NBR 13276 flow-table test. In the CFD simulations, $\tau_{0,CFD} = \tau_{0,A,R}$; K and n were obtained from the Muravleva-based squeeze-flow fitting. The viscosity plateau ν_0 corresponds to the local calibration based on $r(15\ s)$ as a function of $1/\nu_0$ and is treated as a numerical regularization parameter, not as an independently measured material property. The OpenFOAM dictionary uses the kinematic inputs τ_0/ρ and $k = K/\rho$.

Table 3
Materials used in the mortar mixtures and applicable standards.

Component	Standard or description
Fine aggregate (sand)	NBR 7211 (2009) [37]
Binder: common Portland cement CP-II-E-32	NBR 16697 (2018) [38]
Binder: hydrated lime CH-III	NBR 7175 (2002) [39]
Potable mixing water	NM 137 (1997) [40]
FIBRO (ornamental rock processing fines)	No specific standard applies; material described according to IEMA [1] and Neves et al. [3].

Table 4
Water-to-cement ratio (w/c) and designation of the mortars studied.

Series	Mix	Components, dry mass ratio	w/c
R	R30	Hydrated lime : cement : sand = 1:1:6	1.30
	R40		1.40
	R50		1.50
	R60		1.60
	R70		1.70
F	F30	FIBRO : cement : sand = 1:1:6	1.30
	F40		1.40
	F50		1.50
	F60		1.60
	F70		1.70

in the present study by particle-size distribution. Previous studies on similar ornamental rock waste streams from the same regional production context have reported fine particle-size distributions and filler-like behavior in cementitious materials; however, chemical, mineralogical, and morphological characterization of the specific FIBRO batch used here was not performed. This limitation is addressed explicitly in Section 2.5 and considered in the interpretation of the results.

The water-to-cement ratio was varied from 1.30 to 1.70 in both series, as shown in Table 4. These values are higher than those typically adopted for structural mortars, but they are consistent with the 1:1:6 dry proportion, the high fine-particle content of the mixtures, and the need to cover the target spread range around 260 mm. The same w/c levels were used in the R and F series so that the influence of replacing hydrated lime with FIBRO could be evaluated under directly comparable water contents.

2.5. Material characterization and reproducibility strategy

The experimental program focused on the fresh-state response of mortars and on the numerical reproduction of their gravity-driven free spreading. Particle-size distribution was used as the measured physical descriptor of the solid phases, whereas fresh density, flow-table consistency, and squeeze-flow response were used to evaluate the resulting fresh-state behavior.

For the specific FIBRO batch used in this study, chemical, mineralogical, morphological, and particle-shape characterization by X-ray fluorescence (XRF), X-ray diffraction (XRD), scanning electron microscopy (SEM), or image-based shape analysis was not performed. This is an important limitation because ornamental rock processing fines may vary according to rock type, quarry source, sawing or polishing process, and waste-management route. Previous studies on ornamental rock waste streams from the same regional production context have reported fine particle-size distributions, filler-like behavior, and mineralogical compositions compatible with siliceous and carbonate ornamental rocks [4,7,8]. In particular, for an ornamental rock waste fine from the same regional production context (Cachoeiro de Itapemirim, ES), Bahiense et al. [7] reported a textural composition of 9% clay, 66% silt, and 25% sand, a real grain density of 2.86×10^3 kg m^{-3}, and scanning electron micrographs of the raw waste fines, reproduced here as Fig. 4. Chemical and mineralogical reference data from the same regional lineage are available from earlier studies by Bahiense on ornamental rock processing fines from this production region [5,6]. Semi-quantitative X-ray fluorescence (EDX) of two independent batches indicated a predominantly silicate composition, with SiO_2 = 62.2–63.2 wt%, Al_2O_3 = 14.8–16.0 wt%, K_2O = 6.9–7.9 wt%, Fe_2O_3 = 6.0–7.0 wt%, and CaO = 4.6–6.7 wt%, and X-ray diffraction identified quartz, microcline, albite, cordierite, and illite/mica as the main crystalline phases, consistent with acidic (granite/gneiss) source rocks; part of the Fe_2O_3 and CaO contents was attributed to the steel shot and lime used as abrasive and lubricant in block sawing [5,6]. These regional data indicate that FIBRO-type fines are mineralogically distinct from monomineralic inert fillers such as limestone or quartz powder, combining quartz with feldspars and micas and carrying process-derived iron- and calcium-bearing constituents. Because those analyses refer to older batches from the same production region, and because the regional industry processes both silicate and carbonate rocks, they are used here as regional lineage context rather than as direct characterization of the specific FIBRO batch investigated in the present work.

Accordingly, interpretations related to particle packing, filler effect, lubrication, surface morphology, or microstructural mechanisms are formulated cautiously. In this study, a denser granular arrangement is inferred only indirectly from the measured particle-size distribution, the higher fresh density of the FIBRO-containing series, and the lower water-to-cement ratio required to reach the target spread. No direct claim is made regarding particle shape, chemical reactivity, hydration products, or microstructural development of the specific FIBRO batch. Complete physicochemical and morphological characterization is identified as a priority for future work and as a requirement for broader reproducibility across different FIBRO sources.

The consistency index was obtained from three diameter readings for each mixture, following the flow-table procedure. These three readings describe the spread variability within a single test and were used to calculate the mean spread diameter associated with each composition. They should not be interpreted as independent replicate batches. Density, squeeze-flow, and CFD outputs are therefore reported as composition-specific responses, and the uncertainty analysis is limited to descriptive statistics, regression quality, and model-error metrics.

Whenever mean or average values are reported, they are used as descriptive statistics for the corresponding set of mixtures or numerical results. For density comparisons, the sample size corresponds to the number of water-to-cement ratios in each series ($n = 5$). For CFD error metrics, the sample size corresponds to the number of simulated mixtures included in each time-level comparison. No inferential statistical significance testing, such as ANOVA, was performed because independent replicate batches were not available for all responses. Consequently, the results are interpreted as trends within the investigated mix-design route rather than as universal statistical relationships for all FIBRO-containing mortars.

The flow-table tests were recorded on video to distinguish two experimental geometric states. The first frame was extracted immediately after vertical mold removal, before the application of the 30 table drops, and was used to measure the post-mold radius and height. The second frame was extracted after completion of the standardized flow-table procedure and was used to determine the final consistency index. Only the first post-mold frame is physically comparable with the gravity-driven free-spreading simulation, because the CFD model does not include table jolting. Therefore, the numerical radius and height deviations reported in this study are calculated with respect to the post-mold geometric reference, not with respect to the final post-jolting consistency diameter.

Mortar preparation followed the staged mechanical mixing procedure specified in NBR 7215 [41], as adopted for the consistency-test preparation of NBR 13276 [34], using the corresponding planetary mortar mixer. Water and cement were first mixed for 30 s at low speed; the remaining dry fraction was then added gradually over the following 30 s with the mixer kept at low speed; mixing continued for 30 s at high speed; the mixer was then stopped for 90 s, during which the material adhering to the bowl and paddle was scraped down in the first 15 s and the mortar rested covered for the remaining 75 s; a final 60 s stage at high speed completed the procedure, corresponding to approximately 4 min in total from water–cement contact. Molding for the consistency test and the fresh bulk-density determination [42] were performed immediately after mixing, from the same batch and on the same bench; both fresh-state measurements therefore share the same short and controlled post-mixing resting history.

The experimental sequence followed the standardized fresh-state testing workflow. The flow-table test was used to define the consistency response and to provide the final post-jolting spread diameter for the workability analysis. The video frames were then used to extract the post-mold and final geometric states. Squeeze-flow tests were performed on fresh specimens prepared from the corresponding mortar mixtures, using the two standard velocities prescribed by NBR 15839. The low-velocity test was initiated approximately 15 min after mixing, whereas the high-velocity test was initiated approximately 10 min after mixing. These times are reported to make the experimental history explicit, since structural build-up in cementitious materials may depend on the elapsed time after water addition. Together with the mixing protocol described above, they define the complete experimental timeline (mixing history, resting periods, and test start times) relevant to possible structural build-up. No independent time-dependent rheometry was performed; therefore, possible structural evolution is treated as a limitation rather than as a directly measured variable.

2.6. Numerical modeling of gravity-driven free spreading

The CFD simulations were performed in OpenFOAM 13 with the OpenFOAM solver `incompressibleMultiphaseVoF`, executed via `foamRun`. The numerical model represents the gravity-driven free spreading of a mortar volume initially shaped as the truncated cone used in the standardized consistency test. The simulations do not include the mold-lifting dynamics or the dynamic impacts applied during the NBR 13276 flow-table procedure [34]. Therefore, the numerical model should not be interpreted as a complete reproduction of the standardized consistency test. Instead, it is treated as a calibrated free-spreading benchmark initialized from the same mold geometry.

This distinction is central to the interpretation of the numerical results. The final flow-table spread diameter is a terminal dynamic workability index obtained after mold removal and 30 table drops. In contrast, the CFD model describes impact-free spreading under gravity. For this reason, the final post-jolting spread was used only for the consistency and water-demand analysis, whereas the CFD deviation analysis was performed with respect to the post-mold experimental geometric reference extracted from the first video frame immediately after vertical mold removal and before table jolting.

The Roussel-based estimate of the effective yield-stress parameter was also linked to this post-mold geometric reference, rather than to the dynamically excited final flow-table diameter. This choice was adopted because the Roussel relationship is based on slump-type gravity-driven spreading and is not directly equivalent to the Brazilian flow-table procedure with prescribed impacts. Consequently, the resulting τ_0 values are treated as effective estimates used to anchor the rheological parameterization and the CFD input set, not as direct rheometric measurements or as yield-stress values inferred from the final post-jolting consistency diameter.

Table 5 summarizes the numerical setup used in this study.

The surface tension value $\sigma = 0.072\ N\ m^{-1}$ corresponds to the water–air interface at approximately 20 °C and was adopted as a reference value in the absence of experimental data for the specific mortar mixtures. The sensitivity of the simulations to this parameter was not evaluated and is therefore considered a limitation of the numerical setup.

The homogeneous mortar-phase representation is a simplification. Individual particles, particle-scale interactions, local segregation, bleeding, air entrainment, and two-phase particle–fluid effects are not resolved. These assumptions should be considered when interpreting deviations between the numerical results and the post-mold experimental geometric reference.

The Courant number (Co, Eq. (10)) measures the distance a perturbation travels across a numerical cell during a time step, as a function of the local velocity u, the time step Δt, and the cell spacing Δx_i along direction i:

$$Co = \frac{u\,\Delta t}{\Delta x_i}. \tag{10}$$

Following Thiedeitz et al. [21], `maxCo` was set to 0.08, with `maxAlphaCo` = 0.50 for the VoF fraction. These values were adopted to improve temporal resolution and maintain stability during the early and late stages of spreading, when local velocities and interface curvature may vary rapidly.

Tables 6, 7, 8, and 9 summarize the OpenFOAM settings used in the simulations.

The low-shear-rate viscosity plateau ν_0 was calibrated for each mixture during the early spreading stage. The calibration was based on preliminary simulations performed with different ν_0 values, from which the simulated radius at $t = 15$ s was fitted as a function of $1/\nu_0$. A linear fit was then used to estimate the mixture-specific ν_0 value required to match the post-mold experimental geometric reference at 15 s. This procedure provides a reproducible local calibration of the viscosity plateau, but it should not be interpreted as a full sensitivity analysis of the regularization parameter.

Table 5
Summary of the CFD setup for gravity-driven free spreading initialized from the NBR 13276 mold geometry.

Aspect	Description
Software and solver	OpenFOAM 13 with the `incompressibleMultiphaseVoF` solver, run via `foamRun`.
Physical interpretation	Gravity-driven free spreading of a fresh mortar volume. Flow-table impacts and mold-lifting dynamics were not simulated.
Material properties	For each mortar, ρ was obtained from the fresh-density test [42]. The effective yield-stress parameter τ_0 was obtained from a Roussel-based estimate using the post-mold reference radius and fresh density. The squeeze-flow curves [13] were used to obtain effective K and n values compatible with the force–displacement response, as described in Sections 2.2 and 2.3.
Domain geometry	Axisymmetric wedge domain with opening angle 3°, maximum radius $R_{max} = 0.30$ m, and height $H = 0.10$ m [21].
Initial volume	`setFields` initialization as a truncated cone with height 65 mm, bottom radius 62.5 mm, and top radius 40 mm, corresponding to the standard mold geometry [34].
Phase definition and properties	The simulated phases are the mortar phase and air. In the OpenFOAM dictionaries, the internal label `cement` may appear only as a phase name; physically, this phase represents the complete fresh mortar mixture, not cement paste alone. Air properties were kept constant: $\rho_{air} = 1$ kg m^{-3} and $\nu_{air} = 1.48 \times 10^{-5}$ m^2 s^{-1}. For the mortar phase, properties vary with the mixture.
Interface treatment	The mortar–air interface was captured using the volume-of-fluid formulation. The surface tension at the interface was taken as $\sigma = 0.072$ N m^{-1}.
Initial phase field	Initial volume fraction $\alpha_{mortar} = 1$ inside the truncated cone and $\alpha_{mortar} = 0$ in the rest of the domain.
Rheological model	Homogeneous generalized-Newtonian Herschel–Bulkley model in kinematic form, using effective parameters derived from the experimental workflow.
Main outputs	Simulated spreading radius $r(t)$ and height $h(t)$ at selected times, compared with the post-mold experimental geometric reference.

Table 6
Boundary conditions and constant parameters used in the numerical case.

Entity	Condition/Value	Patch(es)/Remarks
Wedge faces	`wedge`	`wedgeBack`, `wedgeFront`; axisymmetric wedge representation.
Walls, velocity	`noSlip`	`wallBottom`, `wallOuter` for **U**.
Walls, pressure	`fixedFluxPressure`	p_{rgh} on `wallBottom` and `wallOuter`.
Free surface, velocity	`pressureInlet OutletVelocity`	**U** on `atmosphere`.
Free surface, pressure	`totalPressure` = 0	p_{rgh} on `atmosphere`.
Axis	`symmetryPlane`	`axisInner`.
Contact angle	90°, when required	Applied to the volume-fraction field at the bottom wall when needed.
Gravity	$\mathbf{g} = (0, 0, -9.81)$ m s^{-2}	Vertical z direction, using the modified pressure field p_{rgh}.

Table 7
Numerical schemes used in `fvSchemes`.

Category	Entry	Setting
Time	`ddtSchemes`	`Euler`, first order.
Gradients	`gradSchemes`	`Gauss linear`.
Interpolation	`interpolation-Schemes`	`linear`.
Surface-normal gradients	`snGradSchemes`	`orthogonal`.
VoF interface α	`div(phi,alpha.*)`	`Gauss vanLeer`.
VoF interface α	`div(phic,alpha.*)`	`Gauss vanLeer`.
VoF interface α	`div(phirb,alpha.*)`	`Gauss interface-Compression`; no additional artificial interface compression coefficient was imposed.
Momentum	`div(phi,U)`	`Gauss linearUpwind grad(U)`.
Momentum	`div(rhoPhi,U)`	`Gauss linearUpwind grad(U)`.
Effective viscosity	`div(muEff*dev2(T(grad(U))))`	`Gauss linear`.

No order-of-magnitude sensitivity analysis using $10\nu_0$ and $100\nu_0$, and no comparison with alternative regularization schemes such as Papanastasiou regularization, were performed in the present study. Therefore, the late-time deviations at 30 and 60 s may still be affected by residual numerical creep in low-shear regions. For this reason, the late-time bias is interpreted as the combined result of regularization, constitutive simplification, and experimental–numerical non-equivalence, not as direct evidence of thixotropy alone. As a partial, simulation-free consistency check, Section 3.7 compares the simulated late-time radii with the analytical stoppage radius implied by the Roussel-based calibration.

The instant $t = 15$ s was selected as an early-stage calibration point because the simulation was intended to reproduce the initial gravity-driven spreading response after mold removal. This choice does not imply that structural build-up is absent at this time; rather, it provides a consistent reference for comparing the subsequent numerical evolution. The simulated results at 30 and 60 s were then used to evaluate the extrapolation behavior of the stationary Herschel–Bulkley model relative to the post-mold experimental geometric reference.

The final rheological and numerical input parameters used for each mixture, including ρ, τ_0, K, n, ν_0, parameter provenance, and fitting indicators, are reported in Table 2. The wet area on the bottom wall and the mortar–air interface were post-processed to obtain the spreading radius as a function of time. Radius and height were evaluated at 15, 30, and 60 s. Because the CFD model does not include the table-jolting stage, the numerical deviations are calculated with respect to the post-mold experimental geometric reference used for the free-spreading benchmark, not with respect to the final post-jolting consistency diameter.

3. Results and discussion

3.1. Particle size distribution and inferred filler effect

Figs. 2 and 3 show the particle-size distributions of sand and FIBRO, respectively. The residue is markedly finer than the natural aggregate,

Table 8
Solvers and parameters used in `fvSolution`.

Item	Option	Typical values/Remarks
Algorithm	`PIMPLE`	`nOuterCorrectors` = 1; `nCorrectors` = 1; `nNonOrthogonalCorrectors` = 0.
Modified pressure	`GAMG`	For p_{rgh}; tolerance = 1×10^{-8}; `relTol` = 1×10^{-2}.
Velocity	`PBiCGStab/DILU`	For **U**, or `GAMG` depending on the case; tolerance = 1×10^{-8}; `relTol` = 1×10^{-1}.
VoF/MULES	–	Moderate corrections in α, with small values of `nAlphaCorr` and `nAlphaSubCycles`.
Interface compression	`cAlpha`	No additional artificial interface compression coefficient was used.

Table 9
Numerical control, parallelization, and execution pipeline.

Topic	Setting	Remarks
Time window	t_{final} = 60 s	Output curves were reported up to 60 s.
Calibration interval	Early spreading stage, t = 15 s	The viscosity plateau ν_0 was calibrated using the simulated radius at 15 s and the post-mold experimental geometric reference.
Time step	$\Delta t_0 = 1 \times 10^{-6}$ s	`adjustTimeStep` = yes.
Courant control	`maxCo` = 0.08; `maxAlphaCo` = 0.50	Controlled according to [21].
Parallelization	`scotch` decomposition	`numberOfSubdomains`=10 in `decomposeParDict`.
Pipeline	Main execution sequence	`blockMesh` → `setFields` → `decomposePar` → `foamRun -parallel`.

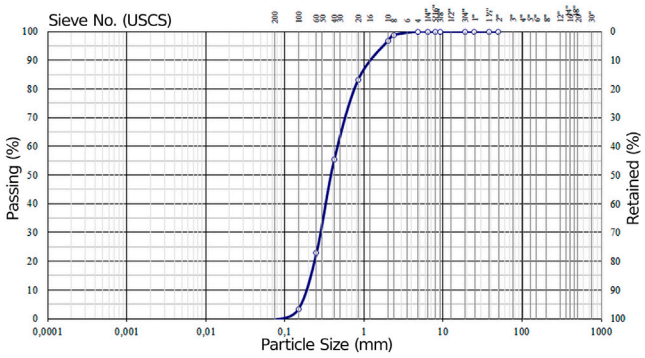


Fig. 2. Particle size distribution of the sand.

with 94% of its particles classified as fines. This contrast in particle-size distribution is relevant because the incorporation of a fine mineral residue into a coarser granular skeleton may contribute to void filling and to a denser fresh-state arrangement when the water content is properly adjusted.

In practical terms, the broader grading of the sand combined with the fine distribution of FIBRO is consistent with the higher fresh density and lower water demand observed for the FIBRO-containing series, as discussed in the following sections. However, this interpretation should be treated as indirect. Particle-size distribution alone does not provide

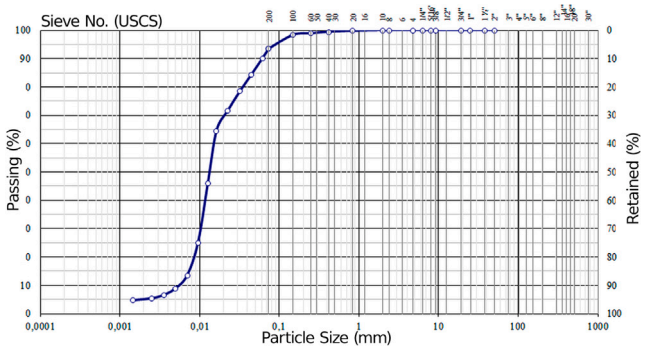


Fig. 3. Particle size distribution of FIBRO (94% fine particles).

a complete description of packing density, particle morphology, surface texture, or chemical/mineralogical composition.

In the present mixtures, FIBRO does not act simply as an inert sand filler. The residue replaced hydrated lime in the dry proportion, while cement and sand contents were kept unchanged. Therefore, the observed fresh-state response may result from the combined effect of fine-particle incorporation, removal of hydrated lime, changes in water retention, and modification of cohesion and plasticity. This replacement route differs from studies in which ornamental stone waste is used as cement or sand replacement, and the results should be interpreted within this specific mix-design framework.

Particle morphology may also affect the rheological response of FIBRO-containing mortars. Angular, lamellar, or rough particles can increase interparticle friction and modify lubrication efficiency, whereas more rounded particles may favor flow [9]. Because particle shape was not directly quantified in the present study, this effect is discussed only as a possible contributing mechanism rather than as an independently measured variable. Similarly, chemical and mineralogical effects cannot be isolated without specific XRF, XRD, or SEM characterization of the FIBRO batch used here.

For visual context, Fig. 4 reproduces scanning electron micrographs of an ornamental rock waste fine from the same regional production context, reported by Bahiense et al. [7]. At these magnifications, the particles appear as angular, irregularly shaped fragments spanning a wide size range, consistent with generation by mechanical sawing and polishing rather than by natural rounding processes. This observation is compatible with the possible lubrication and packing mechanisms discussed above; however, it characterizes a related regional waste stream rather than the specific FIBRO batch used in the present study, and is therefore reported as supporting morphological context rather than as direct evidence.

Recent work on ornamental-rock waste has shown that chemical, mineralogical, and physical heterogeneity should be considered when interpreting the performance of cementitious composites [14]. Therefore, the filler-based interpretation presented here should be understood as a fresh-state mechanism inferred from particle-size distribution, fresh density, and consistency results, and not as a complete mineralogical, morphological, or microstructural characterization of the FIBRO used.

3.2. Higher fresh density associated with FIBRO incorporation

Density measurements performed according to NBR 13278 [42] showed a clear distinction between the two mortar series (Fig. 5). The FIBRO-containing mortars exhibited higher fresh density than the reference mortars over the whole w/c range studied. Considering the five w/c levels in each series, the descriptive mean fresh density was 2327 kg m^{-3} for the F series and 1982 kg m^{-3} for the reference series, corresponding to an average difference of approximately 17%. The

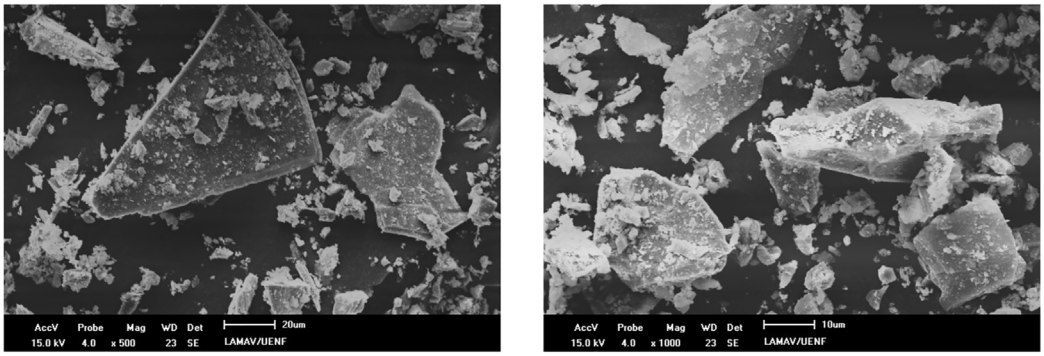


Fig. 4. Scanning electron micrographs of an ornamental rock waste fine from the same regional production context (Cachoeiro de Itapemirim, ES), at (a) 500× and (b) 1000× magnification (reproduced from Figs. 19–20 of Bahiense et al. [7], open access under CC BY 4.0). These images characterize a compositionally similar regional waste stream and are provided as supporting morphological context; they do not represent direct characterization of the specific FIBRO batch investigated in the present study.

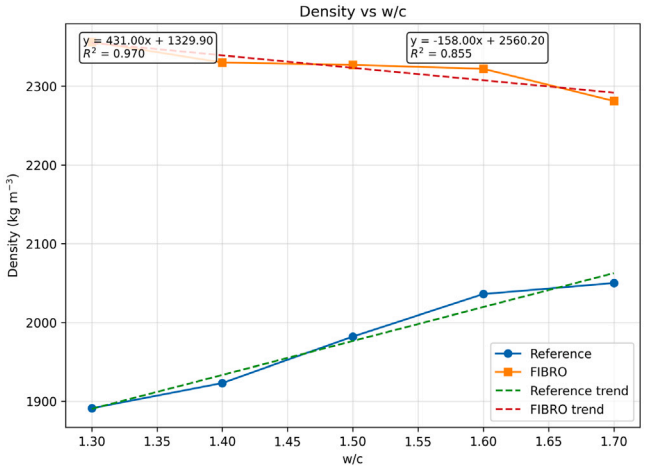


Fig. 5. Fresh density as a function of w/c ratio for the reference and FIBRO mortars.

density–w/c plot also indicates different composition-specific trends: while the reference mortars showed a gradual increase in density with increasing w/c ratio, the FIBRO series remained at a consistently higher density level, with only a slight decrease at higher w/c values.

The higher fresh density of the FIBRO series is consistent with the particle-size contrast discussed in Section 3.1. The fine particle-size distribution of FIBRO may contribute to void filling within the coarser granular skeleton and to a denser fresh-state arrangement when the water content is properly adjusted. Similar particle-packing strategies have been used to design eco-efficient cementitious systems with denser granular skeletons and reduced paste or aggregate demand [43]. However, fresh density should not be interpreted here as a direct measurement of packing density. The observed increase may result from the combined effects of the higher specific gravity of FIBRO relative to hydrated lime (a real grain density of 2.86×10^{3} kg m^{-3} has been reported for a compositionally similar ornamental rock waste fine from the same regional production context [7]), the fine particle-size distribution of the residue, and changes in the fresh granular arrangement caused by replacing the lime fraction.

This distinction is important because FIBRO did not replace cement or sand in the present formulation; it replaced hydrated lime. Therefore, the density increase reflects a specific change in the cement–lime–sand system, rather than a generic filler addition. Replacing hydrated lime with a fine mineral residue may modify not only the solid packing condition, but also water retention, cohesion, and plasticity, which are relevant properties for rendering mortars. From a practical viewpoint, the result indicates that the FIBRO-containing series achieved a denser fresh-state condition while still reaching the target consistency with less water, as discussed in Section 3.3.

Quantitatively, the approximately 17% higher descriptive mean fresh density observed here is larger than the effect usually emphasized in low-level cement-replacement approaches using ornamental stone waste, in which contents close to 10 wt% are often discussed mainly in terms of preserving fresh and hardened performance rather than producing a major density shift [14,19]. This difference is physically reasonable because the present study adopted a different replacement route: FIBRO replaced the hydrated lime fraction in the dry proportion, thereby altering the binder–filler skeleton more strongly than a small cement-replacement level. The result is also compatible with recent studies on waste stone powder fillers, which associate fine mineral additions with changes in packing, rheological response, and compactness [44,45]. Nevertheless, because direct packing-density measurements and particle-shape characterization were not performed, the density response is interpreted as indirect evidence of a modified fresh granular arrangement, not as proof of a specific packing mechanism.

3.3. Consistency index and water demand for target workability

The consistency test was used to compare the water demand required to reach the target terminal spread of 260 mm (Fig. 6). The results indicate that the FIBRO-containing series achieved the target workability with a lower water-to-cement ratio than the reference series. This response should not be interpreted simply as an increase in fluidity. Rather, it reflects the combined effect of the fine particle-size distribution of FIBRO, the replacement of hydrated lime, and the resulting changes in fresh-state density, cohesion, water retention, and interparticle mobility. In this sense, the consistency response is compatible with the higher fresh density observed for the FIBRO mortars.

The relationship between consistency index and water-to-cement ratio was fitted using second-order polynomial interpolations within the experimental range, as shown in Table 10. These equations were used only to estimate the water-to-cement ratio required to reach the target spread of 260 mm. They should not be interpreted as general predictive models for workability outside the tested composition range.

The interpolation results indicate that the FIBRO-containing series required a lower water-to-cement ratio to reach the target consistency index of 260 mm. The estimated w/c decreased from 1.537 for the reference mortar to 1.472 for the FIBRO mortar, corresponding to a reduction of approximately 4.2%. Although modest in relative terms, this reduction is relevant because it was obtained at a fixed target spread rather than by simply increasing the measured flowability.

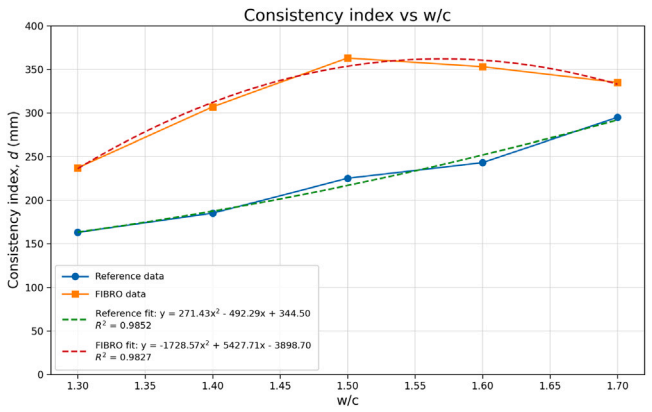


Fig. 6. Consistency index as a function of the water-to-cement ratio for the reference and FIBRO mortars.

Table 10
Polynomial interpolation of consistency index as a function of water-to-cement ratio and estimated w/c required to reach 260 mm.

Mortar	Interpolation equation	R^2	w/c at d = 260 mm
Reference	$d = 271.43x^2 - 492.29x + 344.50$	0.9852	1.537
With FIBRO	$d = -1728.57x^2 + 5427.71x - 3898.70$	0.9827	1.472

d is the consistency index in mm and x is the water-to-cement ratio.

This result is important for fresh mortar design because it links FIBRO incorporation to lower water demand under the adopted mix-design route. In many cementitious systems, very fine additions may increase water demand when the surface-area effect dominates. In the present formulation, however, replacing hydrated lime with FIBRO allowed the target spread to be reached with less water. This behavior suggests that the fine particle-size distribution of the residue and the modified fresh granular arrangement contributed favorably to spreading efficiency. Nevertheless, because particle morphology, surface area, and direct packing density were not measured, this mechanism is interpreted as a plausible explanation supported by particle-size distribution, fresh density, and consistency results, not as a directly demonstrated microstructural mechanism.

The replacement route adopted here also differs from studies in which ornamental stone waste is used as sand or cement replacement. Moreira et al. [18], for example, evaluated mortars with 10, 30, and 60 wt% ornamental-stone processing waste as sand replacement and reported favorable technological and environmental performance for specific replacement levels. In contrast, the present study kept the cement and sand proportions unchanged and replaced the hydrated lime fraction with FIBRO. Therefore, the observed reduction in water demand should be interpreted within this cement–lime–sand formulation, in which changes in lime content, fine-particle distribution, cohesion, and water retention may occur simultaneously.

From a mix-design perspective, the key outcome is that the FIBRO-containing series reached the target terminal spread with an approximately 4.2% lower w/c ratio while also exhibiting higher fresh density. Similar behavior has been reported for cementitious systems containing fine mineral fillers, where particle-size distribution and filler effects may reduce void volume and modify the thickness of the interparticle water film [7,9,43]. However, in the absence of direct packing-density and particle-shape measurements, the denser granular arrangement remains an interpretation consistent with the experimental trends rather than an independently measured packing index.

3.4. Initial yield-stress estimates from the post-mold geometric reference

The application of Roussel's relationship to the post-mold reference radii provided initial estimates of the effective yield-stress parameter for all mixtures, as summarized in Table 2. For the reference series, the estimated values ranged from 496 to 1046 Pa, whereas for the FIBRO-containing series they ranged from 491 to 1282 Pa. These values should be interpreted cautiously. In the present workflow, they are not treated as intrinsic material constants, but as Roussel-based effective estimates used to anchor the subsequent squeeze-flow parameterization and the CFD input set.

The F70 mixture departed from the generally decreasing pattern observed for most of the other mixtures. This response was not removed from the analysis because no independent evidence of experimental error was available. Instead, it is interpreted as an indication that the Roussel-based estimate is sensitive to composition-specific variations in the post-mold geometric response. In the F series, higher water content may modify the balance among fine-particle dispersion, cohesion loss, water retention, and lubrication, especially because FIBRO replaced hydrated lime rather than sand or cement. Thus, the F70 response reinforces the need to treat the Roussel-based values as effective estimates rather than direct measurements.

Because only five water-to-cement levels were investigated in each series, no regression-based relationship was inferred for τ_0 as a function of w/c ratio. The values are therefore discussed as composition-specific effective estimates, reported in Table 2, rather than as predictive trends. Even with these limitations, the estimates provide a physically grounded starting point for parameter identification in the absence of direct rotational rheometry. Their role in the present workflow is methodological: they connect the post-mold geometric reference to the squeeze-flow-based effective Herschel–Bulkley fitting and to the OpenFOAM simulations.

3.5. Squeeze-flow response and Herschel–Bulkley fitting

The Muravleva-based fitting procedure yielded effective Herschel–Bulkley parameters consistent with a strongly shear-thinning response in all mortars, as summarized in Table 2 and illustrated by the fitted curves in Figs. 7 and 8. The fitted flow index n remained below unity for all mixtures, ranging from approximately 0.51 to 0.58, which indicates pseudoplastic behavior within the deformation range considered in the squeeze-flow fitting. The consistency index K was generally higher in the FIBRO-containing series, indicating a higher effective resistance to deformation after yielding.

This apparent contrast indicates that FIBRO did not simply make the mortars more fluid. Instead, replacing hydrated lime with FIBRO modified the effective deformation response of the fresh material. The lower water demand observed in the flow-table test and the higher effective K values obtained from squeeze-flow therefore describe different aspects of workability: the former is related to terminal spread under dynamic flow-table conditions, whereas the latter reflects the force required to deform the material under confined compression.

This response also differs from the behavior reported for cement pastes in which ornamental stone waste was used as partial cement replacement. Scolaro et al. [19] evaluated 10, 20, and 30 wt% replacement of ordinary Portland cement by ornamental stone waste and observed that the 10 wt% paste exhibited yield stress similar to the reference, whereas 20 and 30 wt% reduced yield stress by up to 15%. In the present mortars, however, FIBRO replaced hydrated lime within a cement–lime–sand system, and the rheological parameters were obtained as effective Herschel–Bulkley parameters from squeeze-flow data. Therefore, the higher K values observed in the FIBRO series should not be interpreted as contradicting previous cement-paste results, but as a consequence of a different matrix, replacement route, and parameter-identification method.

The effective parameter set also shows that the relationship between K and the Roussel-based yield-stress estimate τ_0 was not strictly monotonic, particularly in the FIBRO series. Because only five compositions were investigated in each series, no regression-based relationship was used to describe K, n, or K–τ_0 trends. These parameters are instead

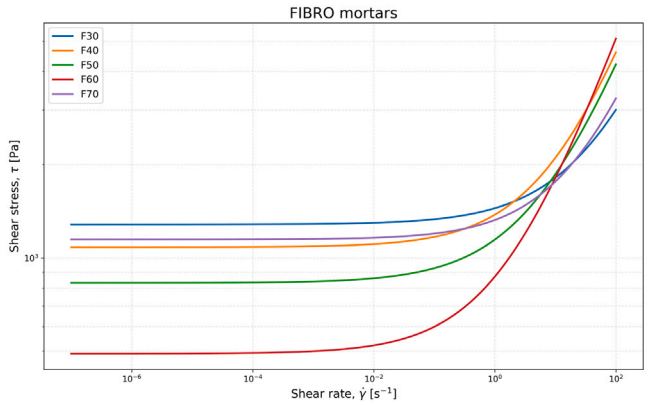


Fig. 7. Fitted Herschel–Bulkley curves for the FIBRO mortars (log–log scale). Effective parameters are listed in Table 2.

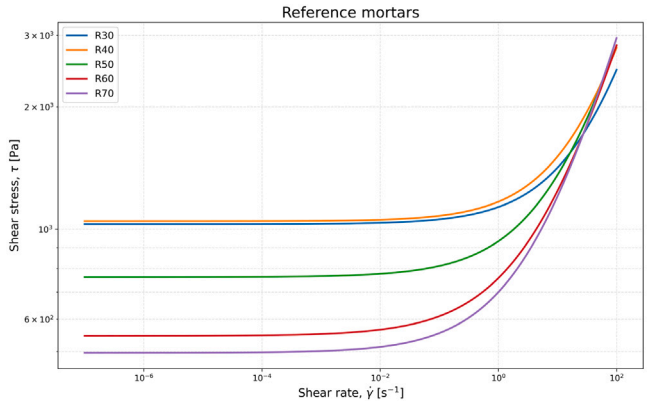


Fig. 8. Fitted Herschel–Bulkley curves for the reference mortars (log–log scale). Effective parameters are listed in Table 2.

treated as composition-specific effective values. This reinforces the interpretation that the yield-stress values obtained from the post-mold geometric reference are useful as physically grounded inputs for the fitting procedure, but should not be interpreted as complete intrinsic rheological measurements. A similar dependence of fitted Bingham and Herschel–Bulkley parameters on the shear-rate fitting window, and its direct propagation into predicted spreading distances, has recently been quantified for cement grouts [28], reinforcing the treatment of τ_0, K, and n as workflow-dependent effective parameters.

The fitted stress–shear-rate curves further illustrate the nonlinear response of both series (Figs. 7 and 8). Within the fitted range, the curves are consistent with a shear-thinning Herschel–Bulkley-type response rather than with a Newtonian behavior. The FIBRO-containing mortars showed higher consistency levels in most cases, while maintaining flow-index values close to those of the reference series. Therefore, the main rheological effect of FIBRO in this parameterization was not a change in flow regime, but a modification of the effective stress scale required to sustain deformation.

For readability, Figs. 7 and 8 show only the mixture labels in the legends, while the corresponding effective parameters τ_0, K, and n are reported in Table 2.

The fact that all fitted values of n remained below unity indicates that the mortars behaved as shear-thinning materials within the fitted deformation range. This is relevant for practical workability because the apparent resistance to deformation decreases under increasing shear rate. However, the parameters should be interpreted as effective values associated with the imposed squeeze-flow and spreading conditions, rather than as universal material constants.

Table 11
`checkMesh` general mesh statistics.

Item	Value
Points	120 801
Faces	240 300
Cells	60 000
Boundary patches	6
Cell types	59800 hexahedra; 200 prisms; other types: 0
Wedge faces	1.5° on `wedgeBack` and `wedgeFront`

Table 12
Mesh quality indicators obtained from `checkMesh`.

Metric	Obtained	Recommended limit	Status
Max. non-orthogonality	0	≤65–70	OK
Max. skewness	0.33242	<4	OK
Max. aspect ratio	6.05393	<10; up to ≤20 tolerated	OK
Max. cell openness	3.11227×10^{-16}	$\ll 10^{-2}$	OK
Face area, min.	1.55518×10^{-8} m^2	>0	OK
Cell volume, min.	1.07746×10^{-11} m^3	>0	OK
Edge length, min.	7.25682×10^{-5} m	>0	OK
Edge length, max.	1.57062×10^{-2} m	>0	OK
Cell determinant, min.	0.520272	>0.1; good practice	OK

This distinction is particularly important for mortars containing fine mineral residues, because particle flocculation, water redistribution, and structural rebuilding may evolve during testing.

The flow-table test alone would indicate that FIBRO improves spreading efficiency at the target consistency. The squeeze-flow analysis adds a complementary interpretation: the residue changes the scale and shape of the force–displacement response and provides effective Herschel–Bulkley parameters that can be used as CFD inputs. Thus, the experimental result is translated into a practical constitutive parameterization, while preserving the limitation that the fitted parameters are test-dependent and should not be generalized beyond the investigated mixtures and deformation conditions.

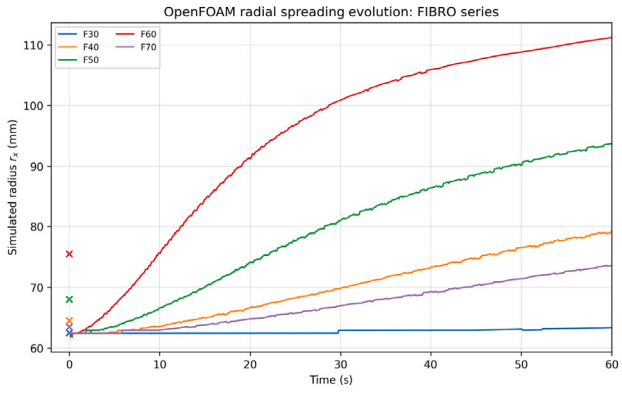
3.6. Numerical stability and mesh adequacy

The numerical results must be interpreted in light of the quality and stability of the computational setup. The wedge mesh satisfied the standard geometric quality criteria reported by `checkMesh`, with zero non-orthogonality, low skewness, positive cell volumes, and an acceptable aspect ratio (Tables 11 and 12). Adaptive time stepping with the prescribed Courant limits also kept the simulations numerically stable throughout the analyzed time window.

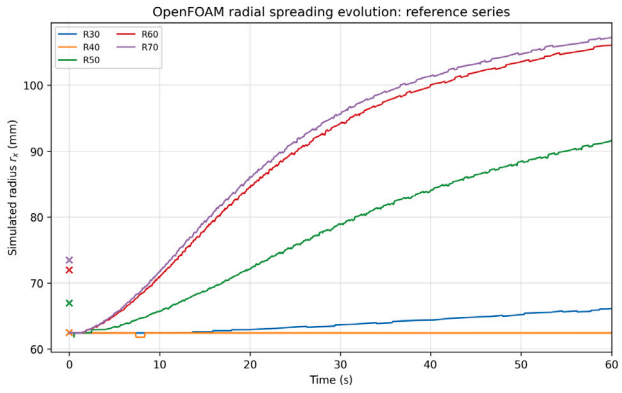
These indicators support the geometric adequacy of the mesh and the numerical stability of the simulations performed in this study. However, they do not constitute a full mesh-independence or time-step-convergence analysis. Therefore, the discrepancies between simulated and experimental spreading are interpreted primarily in terms of constitutive assumptions, input parameterization, numerical regularization, and experimental–numerical non-equivalence, while recognizing that a systematic mesh and time-step sensitivity study would be required for complete numerical verification.

3.7. CFD free-spreading benchmark: early calibration and late-time extrapolation

The OpenFOAM simulations were evaluated as a calibrated gravity-driven free-spreading benchmark, not as a full time-resolved reproduction of the NBR 13276 flow-table test. Two experimental geometric references are used in this study and must be distinguished. The final post-jolting spread diameter was used in the consistency and water-demand analysis. In contrast, the Roussel-based effective yield-stress estimate and the CFD deviation analysis were linked to the post-mold geometric reference extracted from video-frame measurements



(a) FIBRO series



(b) Reference series

Fig. 9. OpenFOAM-predicted radial spreading evolution for the reference and FIBRO mortar series up to 60 s. Curves represent the simulated free-spreading radius $r(t)$. Cross markers indicate the experimental geometric reference extracted from the video-frame measurements used for the CFD comparison; they do not represent time-resolved experimental measurements.

immediately after vertical mold removal and before the 30 table drops. This choice was adopted because the Roussel relationship and the CFD model both refer to gravity-driven spreading conditions, whereas the final flow-table diameter is affected by dynamic excitation.

The same Roussel-based τ_0 values were used as effective material parameters in the CFD simulations. This choice provides a consistent parameterization between the post-mold geometric reference, the squeeze-flow fitting, and the numerical model. However, it also means that the CFD comparison should not be interpreted as a direct reproduction of the complete flow-table procedure. It is a calibrated free-spreading extrapolation using effective parameters estimated from the experimental workflow.

At the calibration instant, $t = 15$ s, the mean absolute relative deviation in radius, computed across the ten simulated mixtures ($n = 10$), was 3.50%. This low value is expected because the viscosity plateau ν_0 was calibrated using the simulated radius at this early spreading stage. Therefore, the 15 s radius agreement should be interpreted as calibration performance rather than independent validation. Height predictions were less accurate at the same instant, with a mean absolute relative deviation of 17.34%, indicating that matching the radial spread does not necessarily ensure accurate reproduction of the vertical profile. As time progressed, the deviations relative to the experimental geometric reference increased: radius deviations rose to 14.80% at 30 s and 26.09% at 60 s, while height deviations increased to 29.17% and 39.16%, respectively.

Fig. 9 shows that the simulated radius was generally close to the post-mold experimental geometric reference at the calibration time.

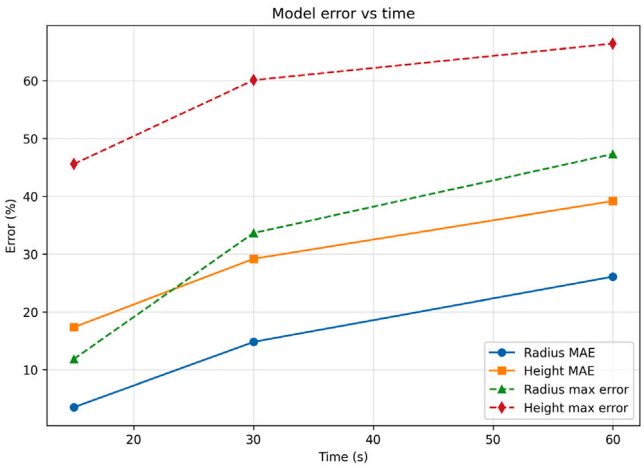


Fig. 10. Time evolution of the mean absolute relative deviation for radius and height predictions, calculated with respect to the experimental geometric reference used for the CFD comparison.

Nevertheless, several mixtures continued spreading substantially up to 60 s, moving progressively away from this reference geometry. This late-time over-spreading is especially evident for F50, F60, R60, and R70, whereas F30 and R40 remained comparatively stable and close to the post-mold reference over the simulated interval.

The deviation evolution in Fig. 10 quantifies this tendency. The dominant numerical pattern was the overestimation of spreading radius combined with the underestimation of height. This behavior indicates that, under the adopted regularization and constitutive assumptions, the simulated mortar remained too mobile after the calibration time. Some mixtures, such as F30 and R40, maintained good agreement throughout the simulated interval, whereas F50, F60, R60, and R70 showed much larger deviations, especially at 30–60 s.

The early radius deviation of 3.50% is comparable to low-error CFD studies on mini-slump and slump-flow simulations, where spreading-radius discrepancies around or below 4%–5% have been reported under calibrated conditions [21,23]. However, the present comparison must be interpreted more cautiously because the numerical model does not include the impacts of the flow table. In addition, the agreement at 15 s results from calibration of ν_0, whereas the 30 and 60 s values test the extrapolation behavior of the same stationary Herschel–Bulkley parameterization. The increase in mean radius deviation to 26.09% at 60 s therefore shows that early calibration does not guarantee late-time predictive accuracy.

A complementary, simulation-free consistency check follows directly from the calibration structure of the workflow and addresses the arrest behavior expected from the effective parameterization. Because $\tau_{0,A,R}$ was estimated from the post-mold reference radius through Eq. (4), the post-mold radius R_{pm} is, by construction, the analytical stoppage radius implied by the calibrated effective yield stress: a purely yield-stress-governed gravity-driven spreading with the same τ_0/ρ should arrest in the vicinity of R_{pm}. Table 13 compares R_{pm} with the simulated radius at 60 s. The exceedance of the simulated radius over the implied stoppage radius decreases essentially monotonically with the kinematic yield parameter τ_0/ρ (Table 2): the three mixtures with the highest τ_0/ρ (F30, R40, R30) remained within about 6% of R_{pm} at 60 s, whereas the mixtures with the lowest τ_0/ρ (R60, R70, F60) exceeded it by 46%–47%. This pattern is consistent with slow residual creep at the imposed viscosity plateau, which prevents a strictly arrested state in the bi-viscosity regularization and acts preferentially on the mixtures whose driving stresses remain closer to the effective yield threshold for longer times. It is also consistent with the mixture-specific ν_0 values reported in Table 2: R40, calibrated with the

Table 13
Analytical stoppage-radius consistency check: post-mold reference radius R_{pm}, which by construction is the arrest radius implied by the Roussel-based calibration of τ_0, versus the simulated spreading radius at 60 s.

Mix	τ_0/ρ (m^2 s^{-2})	R_{pm} (mm)	r_x(60 s) (mm)	$(r_x(60\ s) - R_{pm})/R_{pm}$ (%)
R30	0.543	62.5	66.17	+5.9
R40	0.543	62.5	62.43	−0.1
R50	0.384	67.0	91.61	+36.7
R60	0.268	72.0	106.05	+47.3
R70	0.241	73.5	107.18	+45.8
F30	0.544	62.5	63.37	+1.4
F40	0.464	64.5	79.16	+22.7
F50	0.357	68.0	93.72	+37.8
F60	0.211	75.5	111.19	+47.3
F70	0.502	63.5	73.57	+15.9

R_{pm} and τ_0/ρ are reported in Tables 1 and 2; r_x(60 s) is the simulated free-spreading radius shown in Fig. 9. Because τ_0 was calibrated from R_{pm} through Eq. (4), the relative difference measures how far the regularized stationary model over-runs the arrest radius implied by its own effective yield stress. The mean absolute value of this difference, 26.09%, coincides with the mean radius deviation at 60 s reported above.

largest plateau viscosity, is the only mixture that effectively arrested at its implied stoppage radius. Although this check does not replace an order-of-magnitude sensitivity analysis of ν_0 or a comparison with Papanastasiou-type regularization, it supports the interpretation of the late-time over-spreading as an extrapolation artifact of the regularized stationary model, rather than as evidence of genuinely unbounded spreading or of thixotropy alone.

From a physical and numerical standpoint, the late-time bias is consistent with the limitations of a stationary Herschel–Bulkley law combined with a finite low-shear viscosity plateau. A generalized-Newtonian model with no explicit time dependence cannot represent structural rebuilding, thixotropy, or other time-dependent changes that may occur during periods of low shear or rest. At the same time, the bi-viscosity regularization may allow residual numerical creep in low-shear regions, which can contribute to continued spreading after the material would have effectively stopped in the experimental test. Recent studies on cementitious materials have emphasized that structural build-up and time-dependent rheology can control transient flow response, particularly when the material experiences low-shear periods [46,47].

Thus, the late-time deviations should not be attributed exclusively to thixotropy. They are interpreted here as the combined result of constitutive simplification, numerical regularization, and experimental–numerical non-equivalence. The main numerical contribution of this study is therefore not a complete validation of the flow-table test, but the identification of the time window in which a calibrated stationary Herschel–Bulkley free-spreading simulation remains useful, and the conditions under which its extrapolation becomes unreliable for the mortars investigated.

3.8. Implications for mortar design and model development

Taken together, the results indicate that FIBRO-containing mortars can provide fresh-state advantages within the mix-design route investigated in this study. Replacing hydrated lime with FIBRO produced mortars with higher fresh density and lower water demand to reach the target terminal spread. These results suggest that ornamental rock processing fines may be technically useful in rendering-mortar formulations when the objective is to valorize a mineral residue while maintaining the required fresh workability.

However, these advantages should not be interpreted only from the consistency index. The squeeze-flow results showed that the FIBRO-containing mortars also exhibited a structured shear-thinning response, with effective Herschel–Bulkley parameters that differed from those of the reference series. Therefore, FIBRO did not simply increase fluidity. Instead, it modified the fresh-state response in a way that combines lower water demand under flow-table conditions with higher effective resistance to deformation under squeeze-flow conditions. This distinction is relevant for mortar design because spread diameter alone does not fully describe the material behavior during application.

From a numerical perspective, the combined experimental–computational workflow provides a practical route for converting fresh-state test results into CFD input parameters. The flow-table test supplied the final post-jolting spread used for the consistency and water-demand analysis, while the post-mold geometric reference supported the Roussel-based effective yield-stress estimate used in the numerical workflow. The squeeze-flow fitting supplied effective Herschel–Bulkley parameters for the free-spreading simulations. This integration is more informative than relying on empirical workability measurements alone, because it links mixture composition, rheological parameterization, and numerical response.

At the same time, the simulations showed that the predictive capability of the stationary Herschel–Bulkley framework is time-limited. The calibrated model reproduced the early free-spreading radius with low deviation, but progressively overestimated radius and underestimated height at later times. Therefore, the model is useful as an early-stage calibrated benchmark, but it should not be used as a complete time-resolved representation of the standardized flow-table test. Improved constitutive descriptions, including time-dependent structural build-up and thixotropy-aware models, are required if late-time spreading and arrest are to be predicted more reliably.

3.9. Limitations and future work

The present study was designed to connect standard fresh-state tests, squeeze-flow-based effective rheological fitting, and CFD simulation of gravity-driven free spreading. The results should therefore be interpreted within the limits of this experimental and numerical framework.

First, the packing-related interpretation was inferred from particle-size distribution, fresh density, and consistency response. Direct packing-density measurements, particle-shape analysis, specific surface area, or Andreasen-type packing optimization were not performed. Therefore, the proposed filler and packing effects should be understood as plausible mechanisms supported by fresh-state trends, not as directly measured microstructural evidence.

Second, the chemical, mineralogical, and morphological characterization of the specific FIBRO batch used in this study was limited. SEM morphology, a fuller textural breakdown (clay/silt/sand fractions), and real grain density have been reported for a compositionally similar ornamental rock waste fine from the same regional production context [7] and are used here only as supporting context (Section 3.1, Fig. 4); regional-lineage XRF and XRD data from older batches of the same production region are also available and are summarized in Section 2.5 [5,6], but none of these analyses characterizes the specific batch used here. Future work should therefore include XRF, XRD, SEM, particle-shape analysis, and specific surface area measurements performed directly on the FIBRO batch investigated here, to improve traceability and reproducibility. This is particularly important because ornamental rock processing fines may vary according to quarry source, rock type, processing route, and residue-management practice.

Third, the experimental program did not include independent replicate batches for all measured responses. As a result, the comparisons were treated as composition-specific trends and descriptive statistics, rather than as inferential statistical conclusions. Future studies should include replicated batches and formal uncertainty analysis to support statistical comparison between reference and FIBRO-containing mortars.

Fourth, the numerical model represents gravity-driven free spreading and does not reproduce the complete NBR 13276 flow-table procedure. Mold-lifting dynamics, table impacts, particle-scale effects, segregation, bleeding, and air-entrainment effects were not explicitly

modeled. In addition, the mortar was represented as a homogeneous Herschel–Bulkley material, using effective parameters derived from squeeze-flow. This simplification is useful for a calibrated benchmark, but it cannot capture all physical processes involved in the standardized test.

Finally, the stationary Herschel–Bulkley model and the adopted low-shear viscosity plateau do not explicitly account for structural build-up, thixotropy, or time-dependent changes in the fresh material. The late-time deviations observed in the simulations may therefore result from the combined effects of constitutive simplification, numerical regularization, and experimental–numerical non-equivalence. The analytical stoppage-radius check reported in Section 3.7 partially constrains this interpretation without additional simulations, but it does not replace a formal sensitivity analysis. Future work should combine time-dependent rheometry, sensitivity analysis of the regularization parameter, alternative regularization schemes, mesh and time-step convergence studies, and thixotropy-aware constitutive models to improve the prediction of spreading arrest and late-time free-surface evolution.

4. Conclusions

This study combined fresh-state testing, squeeze-flow-based effective rheological parameterization, and OpenFOAM simulations to investigate cementitious mortars in which hydrated lime was replaced by ornamental rock processing fines (FIBRO). The results support the following conclusions.

First, the FIBRO-containing mortars exhibited a distinct fresh-state response within the investigated mix-design route. Compared with the reference series, the FIBRO series showed a higher descriptive mean fresh density, 2327 kg m^{-3} against 1982 kg m^{-3}, and reached the target terminal spread of 260 mm with an approximately 4.2% lower water-to-cement ratio. This indicates that, under the present formulation, replacing hydrated lime with FIBRO reduced the water demand required to reach the target workability. However, this result should be interpreted within the specific cement–lime–sand system studied here and should not be generalized to all possible FIBRO replacement routes.

Second, the particle-size distribution of FIBRO, together with the fresh density and consistency results, is compatible with a filler-related modification of the fresh granular arrangement. Nevertheless, this interpretation remains indirect. Since direct packing-density measurements, particle-shape analysis, XRF, XRD, SEM, and specific surface area measurements were not performed for the FIBRO batch used in this work, no direct microstructural or mineralogical mechanism is claimed.

Third, the squeeze-flow analysis provided effective Herschel–Bulkley parameters for all mixtures. The fitted flow-index values remained below unity, close to 0.5, indicating shear-thinning behavior within the fitted deformation range. The FIBRO-containing mortars generally showed higher effective consistency-index values than the reference mortars, even though they required less water to reach the target spread. This shows that the effect of FIBRO cannot be described by the flow-table spread alone: the residue modified the effective deformation response of the fresh mortar under squeeze-flow conditions.

Fourth, the OpenFOAM simulations should be interpreted as a calibrated gravity-driven free-spreading benchmark, not as a complete reproduction of the NBR 13276 flow-table test. The numerical model does not include mold-lifting dynamics or table impacts. The CFD comparison and the Roussel-based parameter anchoring were linked to the post-mold geometric reference extracted from the first video frame after mold removal, while the final post-jolting spread was used for the consistency and water-demand analysis. After calibration of the low-shear viscosity plateau at $t = 15$ s, the simulations reproduced the early radial reference with low mean relative deviation. However, this agreement represents calibration performance rather than independent time-resolved validation.

Fifth, the stationary Herschel–Bulkley model showed increasing late-time deviation. Relative to the post-mold geometric reference, radius deviation increased from 3.50% at 15 s to 26.09% at 60 s. The dominant trend was overestimation of radius and underestimation of height, indicating that the simulated material remained too mobile at later times. These deviations should not be attributed exclusively to thixotropy. They are interpreted as the combined result of constitutive simplification, numerical regularization, and experimental–numerical non-equivalence, with possible contribution from time-dependent structural evolution. Consistent with this interpretation, the simulated 60 s radii exceeded the analytical stoppage radius implied by the calibrated effective yield stress in an essentially monotonic pattern with τ_0/ρ, from about 0%–6% for the highest-yield-stress mixtures to about 46%–47% for the lowest.

Overall, FIBRO is a promising residue-valorization route for fresh rendering mortars when used as a hydrated-lime replacement under the conditions investigated in this study. This assessment is limited to fresh-state waste-valorization potential and reduced water demand; life-cycle assessment, durability testing, and hardened-state performance were not evaluated in this study, and broader sustainability claims should await such evidence. At the same time, the results define the limits of using a stationary Herschel–Bulkley CFD model for mortar spreading: the approach is useful for early-stage calibrated free spreading, but late-time spreading and arrest require improved constitutive descriptions. Future work should include replicated batches, complete physicochemical and morphological characterization of FIBRO, direct packing measurements, sensitivity analysis of the regularization parameter, mesh and time-step convergence studies, and time-dependent or thixotropy-aware rheological models.

CRediT authorship contribution statement

M.T. Gabriel: Writing – review & editing, Writing – original draft, Methodology. **A.V. Bahiense:** Resources, Funding acquisition, Conceptualization. **G.C. Xavier:** Supervision, Methodology, Conceptualization. **L.M. Fernandes:** Validation, Supervision, Software, Data curation. **V.P. Della Sagrillo:** Writing – review & editing, Supervision. **M.A. Rabbi:** Supervision, Project administration.

Declaration of Generative AI and AI-assisted technologies in the writing process

During the preparation of this manuscript, the authors used ChatGPT (OpenAI) and Claude (Anthropic) to support language editing, structural checking, and editorial consistency. These tools were not used to generate experimental data, numerical results, or figures. After using these tools, the authors reviewed and edited the content as needed, and they take full responsibility for the content of the publication.

Funding

This study was financed in part by the Coordenação de Aperfeiçoamento de Pessoal de Nível Superior – Brasil (CAPES) – Finance Code 001.

Declaration of competing interest

The authors declare that they have no known competing financial interests or personal relationships that could have appeared to influence the work reported in this paper.

Acknowledgments

The authors thank the collaborators from IFES, UFV, UENF, UFES, Cetemag, and Sindirochas for their support.

Data availability

The data and code supporting the findings of this study are available in Mendeley Data at https://doi.org/10.17632/vfxk7tfzxg.1.

References

[1] Instituto Estadual de Meio Ambiente e Recursos Hídricos (IEMA-ES), Instrução normativa n. 12-n, de 22 de agosto de 2023: dispõe sobre critérios e procedimentos técnicos para o licenciamento ambiental de empreendimentos que exercem as atividades de beneficiamento de rochas ornamentais, 2023.

[2] Associação Brasileira de Normas Técnicas, NBR 15012: Rochas para revestimentos de edificações: Terminologia, 2013, Rio de Janeiro: ABNT.

[3] M.A. Neves, T.S.A. Silva, L.H.S. Oliveira, et al., Lama do beneficiamento de rochas ornamentais (LBRO): Caracterização e possibilidades de aproveitamento, Geociências (UNESP) 40 (2) (2021).

[4] A.L. Paes, J. Alexandre, G.C. Xavier, S.N. Monteiro, A.R.G. Azevedo, Feasibility analysis of mortar development with ornamental rock waste for coating application by mechanized projection, Sustainability 14 (9) (2022) 5101, http://dx.doi.org/10.3390/su14095101.

[5] A.V. Bahiense, Incorporação de resíduo de rocha ornamental em argamassas utilizando planejamento de experimentos em rede simplex, (Master's dissertation, in Portuguese), Campos dos Goytacazes: Universidade Estadual do Norte Fluminense Darcy Ribeiro (UENF), 2007.

[6] A.V. Bahiense, Pavimentos intertravados de matriz cimentícea incorporados com lama do beneficiamento de rochas ornamentais, (Doctoral thesis, in Portuguese), Universidade Estadual do Norte Fluminense Darcy Ribeiro (UENF), Campos dos Goytacazes, 2011.

[7] A.V. Bahiense, J. Alexandre, G.C. Xavier, A.R.G. Azevedo, S.N. Monteiro, Dosage of interlocking paving with ornamental rock waste: An experimental design approach, particle packing and polluting potential, Case Stud. Constr. Mater. 15 (2021) e00596, http://dx.doi.org/10.1016/j.cscm.2021.e00596.

[8] L.F. Amaral, G.C. Girondi Delaqua, M. Nicolite, M.T. Marvila, A.R.G. Azevedo, J. Alexandre, C.M.F. Vieira, S.N. Monteiro, Eco-friendly mortars with addition of ornamental stone waste: A mathematical model approach for granulometric optimization, J. Clean Prod. 248 (2020) 119283, http://dx.doi.org/10.1016/j.jclepro.2019.119283.

[9] X. He, Y. Fang, Y. Peng, W. Shen, D. Qiao, M. Wang, Mortar's rheological property and workability investigation based on morphology impact factor for graded sand particles, Constr. Build. Mater. 328 (2022) 126987, http://dx.doi.org/10.1016/j.conbuildmat.2022.126987.

[10] N. Shanmugasundaram, S. Praveenkumar, Influence of supplementary cementitious materials, curing conditions and mixing ratios on fresh and mechanical properties of engineered cementitious composites: A review, Constr. Build Mater. 309 (2021) 125038, http://dx.doi.org/10.1016/j.conbuildmat.2021.125038.

[11] ASTM International, ASTM C1180-22: Standard Terminology of Mortar and Grout for Unit Masonry, ASTM International, West Conshohocken, PA, 2022, http://dx.doi.org/10.1520/C1180-22.

[12] V.Y. Sato, A.P.L. Galina, J.E.S.L. Teixeira, Contribution to the rheological study of cementitious pastes with addition of residues from the processing of ornamental rocks, Rev. IBRACON Estrut. Mater. 11 (6) (2018) 1284–1307, http://dx.doi.org/10.1590/S1983-41952018000600007.

[13] Associação Brasileira de Normas Técnicas, NBR 15839: Argamassa de assentamento e revestimento de paredes e tetos – caracterização reológica pelo método squeeze-flow, 2010, Rio de Janeiro: ABNT.

[14] B.S. Almada, L.S. Melo, G.J.B. Silva, W.J. Santos, M.T.P. Aguilar, Effect of the waste ornamental rocks on the hydration and life cycle of portland cement composites, Constr. Build. Mater. 395 (2023) 132353, http://dx.doi.org/10.1016/j.conbuildmat.2023.132353.

[15] J.M. Abed, Al-Gburi M, A. Almssad, Evaluation of physical and mechanical properties of modified cement-lime mortar containing recycled granite powder waste as a partial fine aggregate replacement, Appl. Sci. 14 (22) (2024) 10146, http://dx.doi.org/10.3390/app142210146.

[16] M. Farih, O. Chaalal, W.S.K. Abudaqqa, B. Messaoud, An experimental study on the rheological properties of self-consolidating mortars affected by superplasticizer, waste marble powder, and a viscosity-modifying agent, Civ. Eng. Arch. 12 (6) (2024) 4045–4055, http://dx.doi.org/10.13189/cea.2024.120620.

[17] A. Moreno, C. Ponce, E. Múzquiz, F. Avalos, Marble residues in construction materials: A review of the use of marble powder in mortars, concrete, and bricks, Rev. ALCONPAT 12 (2) (2022) 162–183, http://dx.doi.org/10.21041/ra.v12i2.522.

[18] P.I. Moreira, A.R.G. Azevedo, J. Alexandre, G.C. Xavier, S.N. Monteiro, Ornamental stone processing waste incorporated in the production of mortars: Technological influence and environmental performance analysis, Sustain. 14 (2022) 5904, http://dx.doi.org/10.3390/su14105904.

[19] T.P. Scolaro, P.R. Matos, R.A. Schankoski, L.R. Prudencio Jr, Effect of ornamental stone waste incorporation on the rheology, hydration, microstructure, and CO_2 emissions of ordinary Portland cement, Mater. 15 (2022) 401, http://dx.doi.org/10.3390/ma15020401.

[20] J. Engmann, C. Servais, A.S. Burbidge, Squeeze flow theory and applications to rheometry: A review, J. Non-Newton. Fluid Mech. 132 (1–3) (2005) 1–27, http://dx.doi.org/10.1016/j.jnnfm.2005.08.007.

[21] M. Thiedeitz, T. Kränkel, D. Kartal, J.J. Timothy, The slump flow of cementitious pastes: Simulation vs. experiments, Mater. 17 (2) (2024) 532, http://dx.doi.org/10.3390/ma17020532.

[22] K. Vasilic, A. Gram, J.E. Wallevik, Numerical simulation of fresh concrete flow: Insight and challenges, RILEM Tech. Lett. 4 (2019) 57–66, http://dx.doi.org/10.21809/rilemtechlett.2019.92.

[23] J. Němeček, Numerical simulation of slump flow test of cement paste composites, Acta Polytech CTU Proc. 30 (2021) 58–62, http://dx.doi.org/10.14311/APP.2021.30.0058.

[24] M.A. Haustein, M. Eslami Pirharati, S. Fataei, D. Ivanov, D. Jara Heredia, N. Kijanski, D. Lowke, V. Mechtcherine, D. Rostan, T. Schäfer, C. Schilde, H. Steeb, R. Schwarze, Benchmark simulations of dense suspensions flow using computational fluid dynamics, Front. Mater. 9 (2022) 874144, http://dx.doi.org/10.3389/fmats.2022.874144.

[25] T. Jirout, A. Krupica, A. Kolomijec, CFD analysis of ultra-high-performance concrete rheological tests, Fluids 9 (2) (2024) 45, http://dx.doi.org/10.3390/fluids9020045.

[26] W. Chen, W. Wu, G. Lu, G. Tian, Simulation analysis of concrete pumping based on smooth particle hydrodynamics and discrete elements method coupling, Mater. 15 (12) (2022) 4294, http://dx.doi.org/10.3390/ma15124294.

[27] H. Duan, Y. Xie, L. Zou, B. Li, U. Håkansson, V. Cvetkovic, Analysis of grout radial propagation in water-saturated rough-walled rock fractures, Int. J. Rock Mech. Min. Sci. 190 (2025) 106101, http://dx.doi.org/10.1016/j.ijrmms.2025.106101.

[28] H. Duan, L. Zou, B. Li, U. Håkansson, V. Cvetkovic, Effect of rheological model selection on prediction of cement grout propagation in rock fractures, Int. J. Rock Mech. Min. Sci. 202 (2026) 106523, http://dx.doi.org/10.1016/j.ijrmms.2026.106523.

[29] L. Silvestro, A.S. Ruviaro, G. Lima, L.U.D. Tambara Júnior, D. Feys, A.P. Kirchheim, Rotational rheometry test of portland cement-based materials: A systematic literature review, Constr. Build. Mater. 432 (2024) 136667, http://dx.doi.org/10.1016/j.conbuildmat.2024.136667.

[30] R.P. Chhabra, J.F. Richardson, Non-Newtonian Flow and Applied Rheology, second ed. Butterworth-Heinemann, Oxford, 2008.

[31] T.C. Papanastasiou, Flows of materials with yield, J. Rheol. 31 (5) (1987) 385–404, http://dx.doi.org/10.1122/1.549926.

[32] OpenFOAM Foundation, OpenFOAM v13 user guide, 2025, https://doc.cfd.direct/openfoam/user-guide-v13/.

[33] N. Roussel, C. Stefani, R. Leroy, From mini-cone test to abrams cone test: Measurement of cement-based materials yield stress using slump tests, Cem. Concr. Res. 35 (5) (2005) 817–822, http://dx.doi.org/10.1016/j.cemconres.2004.07.032.

[34] Associação Brasileira de Normas Técnicas, NBR 13276: Argamassa para assentamento e revestimento de paredes e tetos: determinação do índice de consistência, 2016, Rio de Janeiro: ABNT.

[35] L. Muravleva, Axisymmetric squeeze flow of a Herschel–Bulkley medium, J. Non-Newton. Fluid Mech. 271 (2019) 104147, http://dx.doi.org/10.1016/j.jnnfm.2019.104147.

[36] J.D. Sherwood, D. Durban, Squeeze-flow of a Herschel–Bulkley fluid, J. Non-Newton. Fluid Mech. 77 (1–2) (1998) 115–121, http://dx.doi.org/10.1016/S0377-0257(97)00099-2.

[37] Associação Brasileira de Normas Técnicas, NBR 7211: Agregados para concreto – especificação, 2009, Rio de Janeiro: ABNT.

[38] Associação Brasileira de Normas Técnicas, NBR 16697: Cimento portland – requisitos, 2018, Rio de Janeiro: ABNT.

[39] Associação Brasileira de Normas Técnicas, NBR 7175: Cal hidratada para argamassas – requisitos, 2002, Rio de Janeiro: ABNT.

[40] Associação Brasileira de Normas Técnicas, NM 137: Argamassa e concreto – água para amassamento e cura de argamassa e concreto de cimento portland, 1997, Rio de Janeiro: ABNT.

[41] Associação Brasileira de Normas Técnicas, NBR 7215: Cimento Portland – Determinação da resistência à compressão de corpos de prova cilíndricos, 2019, Rio de Janeiro: ABNT.

[42] Associação Brasileira de Normas Técnicas, NBR 13278: Argamassa de assentamento e revestimento de paredes e tetos – determinação da densidade de massa e do teor de ar incorporado, 2005, Rio de Janeiro: ABNT.

[43] P. Heidari, P. Rivard, W. Wilson, Multi-objective optimization of cement-based systems containing marine dredged sediment, Constr. Build. Mater. 439 (2024) 137228, http://dx.doi.org/10.1016/j.conbuildmat.2024.137228.

[44] D. Xie, Q. Liu, Z. Zhou, J. Gao, C. Liu, Rheology and hardened properties of eco-friendly ultra-high performance concrete paste: Role of waste stone powder fillers, Constr. Build. Mater. 447 (2024) 138163, http://dx.doi.org/10.1016/j.conbuildmat.2024.138163.

[45] Y. Xie, Y. Jiang, J. Wang, J. Sun, J. Du, H. Zhou, Z. Gong, Y. Hu, Effect of waste granite stone powder content on the rheological and hydration properties of titanium gypsum-based supersulfated cement, Constr. Build. Mater. 478 (2025) 143457, http://dx.doi.org/10.1016/j.conbuildmat.2025.143457.

[46] D. Jiao, R. De Schryver, C. Shi, G. De Schutter, Thixotropic structural build-up of cement-based materials: A state-of-the-art review, Cem. Concr. Compos. 122 (2021) 104152, http://dx.doi.org/10.1016/j.cemconcomp.2021.104152.

[47] H. Varela, G. Barluenga, A. Perrot, Extrusion and structural build-up of 3D printing cement pastes with fly ash, nanoclays and VMAs, Cem. Concr. Compos. 142 (2023) 105217, http://dx.doi.org/10.1016/j.cemconcomp.2023.105217.